12^{th} International Conference on Fracture Mechanics of Concrete and Concrete Structures
FraMCoS-12
B.L.A. Pichler, Ch. Hellmich, P. Preinstorfer (Eds)

https://doi.org/10.21012/FC12.1183
MS03-3:2

CHARACTERISING FLEXURAL BEHAVIOUR OF COARSE AGGREGATE-BASED 3D PRINTED CONCRETE BEAMS USING ACOUSTIC EMISSION TECHNIQUE

SWAPNIL BALASAHEB GHODKE*, SHUBHANKAR ROY CHOWDHURY† AND BHUPINDER SINGH‡

* Research Scholar, Indian Institute of Technology, Roorkee, India
e-mail: swapnilb_ghodke@ce.iitr.ac.in

† Assistant Professor, Indian Institute of Technology, Roorkee, India
e-mail: shubhankar.rc@ce.iitr.ac.in

‡ Professor, Indian Institute of Technology, Roorkee, India
e-mail: bhupinder.singh@ce.iitr.ac.in

Key words: 3D Concrete Printing, Acoustic Emission, Flexural Behaviour, Coarse Aggregates, Sustainability

Abstract. Extrusion-based 3D concrete printing is one of the most popular additive manufacturing techniques in the construction industry, where layer-by-layer structures form. For the 3DCP, most of the researchers use cement mortars of different configurations to the almost total exclusion of aggregates. Although the rheology of cement mortars may make them more amenable to 3D printing, the absence of coarse aggregate fraction in this material makes it more susceptible to the baleful effects of time-dependent phenomena like creep and shrinkage while at the same time, compromising elastic properties of the material and increasing the cement consumption. Incorporating coarse aggregates in 3D printable concrete is one of the ways for the construction industry to achieve sustainability and overcome these problems. This study examines the flexural performance of printed beams through acoustic emission (AE) monitoring to record real-time damage progression during loading. The specimens under examination include coarse aggregate-based printed beams in comparison with mortar-based printed beams in different orientations with respect to the printing direction. The analysis focuses on the evaluation of various AE parameters such as rise time, count, duration and amplitude. The study indicates that the inclusion of coarse aggregates reduces the anisotropic behaviour of printed specimens to some extent. Further, the study found that the AE signals can be effectively used to identify the initiation and propagation of cracks in the printed specimens.

1 INTRODUCTION

The traditional construction sector is currently integrating innovative technology such as 3D concrete printing (3DCP) to address the challenges of skilled labour shortages, formwork, waste, and environmental concerns. The majority of efforts are directed towards the establishment of a sustainable construction sector. Considering such aspects, 3D concrete printing has gained significant popularity over the past decade [1]. 3D concrete printing is an additive manufacturing process which allows construction layer by layer. Khoshnevis et al. [2] was the first who introduce 3D concrete printing in the construction sector via the contour crafting

method. After that, several studies are going on its fresh and hardened properties, reinforcement strategies, optimisation techniques, etc. [1, 3].

Still, 3DCP has not achieved its full potential, primarily due to limitations such as the availability of suitable equipment for incorporating coarse aggregates, its anisotropic behaviour, and lack of understanding of its rheology and hardened properties [4]. Although the name indicates concrete, most of the studies were available on mortar-based printing, resulting in high consumption of cement in current practices, which violates its sustainability aspect. Higher usage of cement creates several more problems, such as an increase in the risk of time-dependent properties creep and shrinkage, an increase in overall material cost and several other durability problems [5, 6]. These issues constrain the use of this technology for practical applications. The inclusion of coarse aggregates not only overcomes these issues it also improves printed structures interlayer bonding.

Few studies [4, 5, 7] are available on the coarse aggregate-based printing and characterization of their hardened properties. Based on the studies, it is found that the hardened properties mainly depend upon the number of layers, loading direction and interlayer bonding. This paper primarily focuses on the analysis of the flexure behaviour of coarse aggregate based notched and unnotched printed beams and its characterization by using the acoustic emission technique. While AE has shown great potential for such analyses, its application to coarse aggregate-based 3DCP remains underexplored. Addressing this gap, the study aims to provide insights into the flexural behaviour of coarse aggregate-based printed beams through AE characterization.

2 METHODOLOGY

2.1 MIX DESIGN

Ordinary Portland Cement (OPC) of 43 grade serves as the principal binder, supplemented by fly ash and silica fume. The fine aggregate and coarse aggregate utilized in this investigation were sourced from river sand and quarry stone, respectively. The dimensions of the fine aggregate range from 0 to 4.75 mm, whereas the coarse aggregate ranges from 4.75 to 10 mm. Their physical properties are shown in Table 1. In addition to this, PCE-based superplasticizers as a water-reducing agent and hydroxypropyl methylcellulose (HPMC) as viscosity modification agents were used to improve the printability properties. The water-to-binder ratio of 0.35 was kept constant for all the mixes. The printable concrete mixes were obtained by the volume replacement of fine aggregate or sand with coarse aggregates (0 to 15%). The detailed mix design is shown in Table 2.

Table 1: Physical properties of aggregates

Properties	Sand	Coarse Aggregate
Fineness Modulus	2.914	-
Water absorption (%)	7.691	3.885
Bulk Density (kg/m^3)	1742.6	1234.1
Specific Gravity	2.677	2.575

Table 2: Mix proportion of 3D printing concrete (kg/m^3)

Mix	Mix 1	Mix 2	Mix 3	Mix 4
C	587	587	587	587
FA	130	130	130	130
SF	33.85	33.85	33.85	33.85
Sand	1296.88	1232.01	1167.18	1102.33
NCA	0	64.84	129.69	194.49
SP	5.6517	5.1803	4.2376	3.7662
VMA	0.7884	0.7884	0.7884	0.7884
W	260.52	260.52	260.52	260.52

2.2 SPECIMEN PREPARATION

The prismatic mortar and concrete specimens were fabricated in dimensions of 450 mm x 250 mm x 150 mm utilizing the gantry-type printer available at the Indian Institute of Technology, Roorkee, India. All the prisms were cured for a duration of 28 days. Additionally, each prism was divided into two segments measuring 350 mm x 120 mm x 120 mm and read-

ied for flexural and testing in both perpendicular and lateral loading directions. In the fracture investigation, beams with a 15% substitution of fine aggregate with coarse aggregate were manufactured, maintaining uniform dimensions and incorporating a notch that is 3 mm wide and 15 mm deep, corresponding to the height of a single printed layer. The printing to specimen preparation process is shown in the Figure 1.

Figure 1: Beam printing to testing process

2.3 TESTING and INSTRUMENTATION

All the specimens for flexure and fracture were tested for a four-point bending test using the Heico servo-controlled 300 kN capacity machine [8]. The four-point bending test setup is illustrated in Figure 2. The testing employs the displacement control method at a loading rate of 0.05 mm/min, as previously established in [9]. The tests continued until a beam failure occurred. To further analyze the flexural and fracture behavior of printed beams, the acoustic emission technique has been employed. Six R6I sensors were firmly positioned at appropriate locations on the surface of the printed beams utilizing silicon grease as a coupling agent, and the acoustic emission signals were recorded during the four-point bending test. The schematic diagram illustrating the sensor positions and their geometric coordinates is presented in Figure 2 and Table 3, respectively. The identical arrangement of AE sensors was employed to evaluate the beams under both perpendicular (orthogonal to the direction of printing: O-I) and lateral (lateral direction to the printing: O-II) loading orientations for the flexural and fracture analysis. A threshold value of 40 dB was established for the AE acquisition system to guarantee a strong signal-to-noise ratio. The sensitivity and coupling of the acoustic emission sensors are assessed using a Hsu-Nielsen source (pencil-lead break) [10].

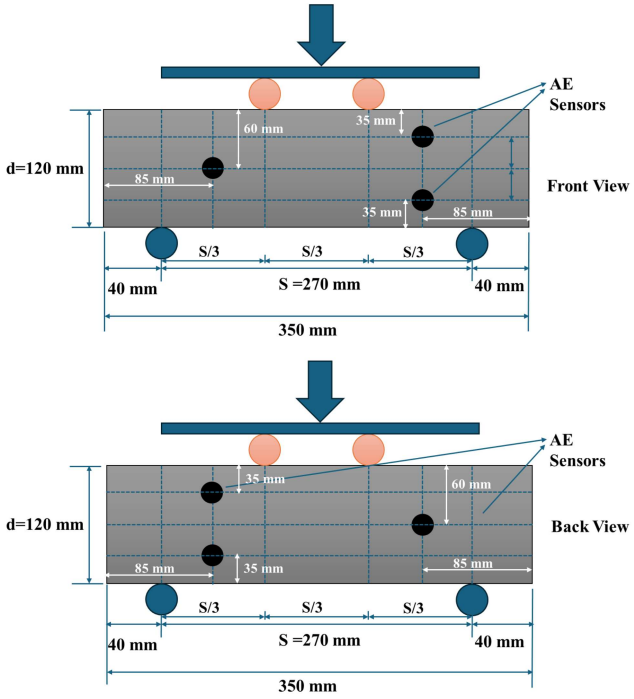

Figure 2: AE sensors arrangement for the testing of flexural behaviour

Table 3: Geometric coordinates of the AE sensors

Sensor No.	X	Y	Z
1	85	60	0
2	265	35	0
3	265	85	0
4	85	35	120
5	85	85	120
6	265	60	120

3 RESULTS and DISCUSSIONS

This section analyzes the flexural acoustic emission data obtained from the testing of mortar and coarse aggregate-based printed beams subjected to flexural load with different loading orientations.

3.1 Load Deflection Characteristics

All the studied specimens demonstrate failure at varying peak loads, influenced by loading orientation and coarse aggregate concentration. The maximum load values of the tested specimens are presented in Table 4. In every instance, peak load values are higher in the loading direction O-II. For Mix 1 (0 % CA), the peak load in the O-II direction is 38.62% greater, whereas for Mix 2 (5% CA), Mix 3 (10% CA), and Mix 4 (15% CA), the increases are 12.35%, 10.12%, and 3.32%, respectively. In the case of Mix 4 (15% CA) notch beams, the variation in peak load across different loading directions is minimal, i.e. 0.53%. Analysis of the peak load values reveals that the increase in coarse aggregate content reduces printed specimen's anisotropic behaviour to some extent. Further, to understand the deflection behaviour, load versus displacement plots are presented in Figure 3. The smaller linear portion of all plots indicates the uncracked condition of the beams. Within this particular zone, the vertical deflection is directly proportional to the load that is being applied, and the entire concrete section is considered to be effective in resisting the loads for the entire region. As seen the Figure 3, the Mix 1 (0 % CA) and Mix 4 (15% CA) based printed beams indicate the higher slopes of the load-deflection curve in the loading direction O-II, whereas other coarse aggregate-based beams show the smaller slope in this direction. The displacement curves might not represent exact central displacement due to the sudden change in displacement observed in the last unit of time. The post-peak of the load-displacement graph is described here only to indicate that brittle failure happens. Here, we are only concerned with the peak load of the tested specimens.

3.2 Flexural Strength

Further, the flexural strength in both directions is calculated according to the IS 516 (Part 1) 2021 [11]. Figure 4 illustrates the flexural strength values of all with and without notch-tested samples under flexure in both directions. In all investigated specimens, flexural strength is seen to be more significant in the lateral direction (orientation-II). The difference in flexural strength between the two orientations is more pronounced in the mortar sample and diminishes as the coarse aggregate concentration increases.

Table 4: Flexural test results

Type of Beams	Orientation	Peak Load
Mix 1 beams	O-I	14.06 kN
	O-II	19.49 kN
Mix 2 beams	O-I	18.86kN
	O-II	21.19kN
Mix 3 beams	O-I	22.83 kN
	O-II	25.14 kN
Mix 4 beams	O-I	21.42 kN
	O-II	22.13 kN
Mix 4 N beams	O-I	13.01 kN
	O-II	13.08 kN

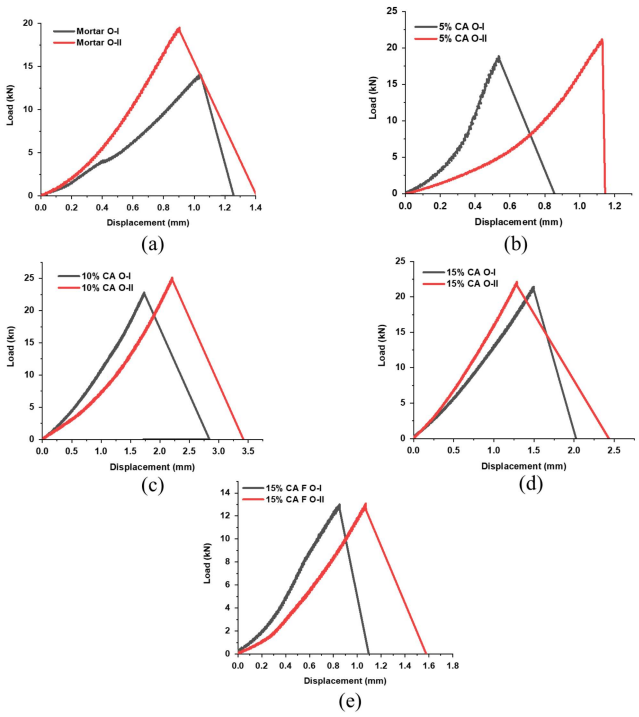

Figure 3: Load versus displacement plots a) Mix 1 beams b) Mix 2 beams c) Mix 3 beams d) Mix 4 beams e) Mix 4 N beams

This decrease may be attributed to the rise in interlayer bond strength due to the increase in

coarse aggregate content, and the same has also been observed in previous literature [12, 13]. Coarse aggregate-based specimens have greater flexural strength than the mortar samples, and it also increases with increasing coarse aggregate content, except in 15% CA specimens. The increase in flexural strength is attributed to enhanced crack resistance and fracture behaviour resulting from the bridging impact of coarse aggregates [14]. Despite the absence of a growing trend with 15% CA addition, it exhibits superior flexural strength compared to mortar-based specimens. The fluctuation in trend may be attributed to alterations in optical packing density and void content. Moreover, Mix 4 beams (15% CA) without notches exhibited superior load-carrying performance in comparison to notched beams. The absence of a notch in these beams resulted in no initial stress field, necessitating a significantly greater load to begin cracks compared to Mix 4 (15% CA) with a notched beam.

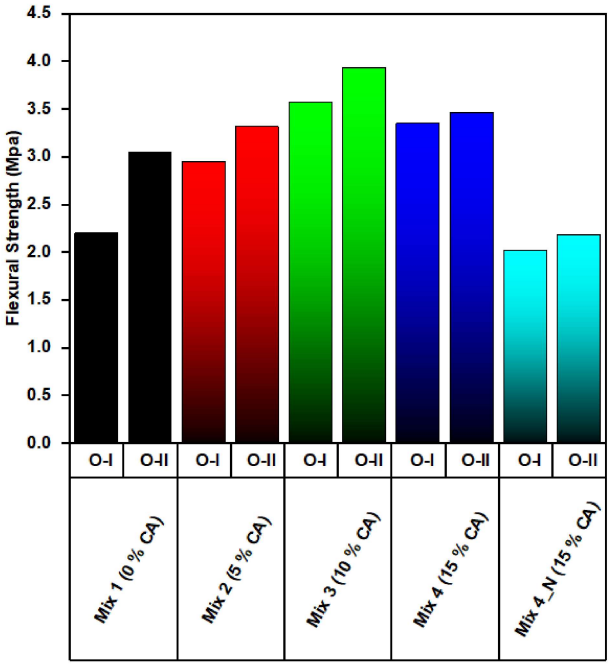

Figure 4: Flexural strength in two different loading directions

3.3 AE Characterisation

This section gives the analysis of monitored AE parameters during both directions of flexural testing. The study indicates the crack propagation in terms of micro and macro cracking in mortar and coarse aggregate-based printed beams according to their loading directions. Figures 5, 6, 7, 8 and 10 illustrate the plots of increase in cumulative AE hits, a sudden rise in cumulative signal strength-curve, cumulative absolute energy-curve and variation of the amplitude of AE hits with increasing flexural loading in mortar and coarse aggregate based printed beams along with load-time curve. It indicates the progression of fracture or cracking in the beams from initiation of cracking to the ultimate brittle failure of these beams. In all the figures, Roman numbers I and II indicate the micro-cracking phase and macro-cracking phase, respectively.

3.3.1 Phase I

An increase in the slope of the cumulative AE hits was observed in all the beams in both O-I and O-II loading directions, which indicates the starting point of the AE activity inside the beam in the form of micro-cracking. The sudden rise or knee formation in the plots of cumulative signal strength and cumulative absolute energy also supports this. A similar pattern is also observed in plots of Mix 4 (15% CA) notched beams (see Figure 10). For loading direction along orientation-I (O-I), the duration of the micro-cracking phase is 650 sec, 460 sec, 1150 sec, and 1300 sec for 0% CA-based, 5% CA-based, 10% CA-based, and 15% CA-based beams, respectively. In the case of loading orientation-II (O-II), the durations are 830 seconds, 1100 seconds, 2100 seconds, and 910 seconds, respectively. Whereas in the case of 15% CA-based notched beams, the duration of the micro-cracking phase is decreased compared to without notch beams and observed as 670 sec for loading in orientation-I and 820 sec for loading in orientation-II. The reduced dura-

tion of the micro-cracking phase in 15% CA-based notched beams is primarily due to the notch acting as a stress concentrator, leading to faster crack localization and propagation. The presence of coarse aggregates influences the stress distribution and crack-bridging effects, but the notch dominates the failure mechanism, shortening the micro-cracking phase compared to unnotched beams [15].

Likewise, an increase in coarse aggregate (CA) content correlates with an extended length of the micro-cracking phase for unnotched beams (except 5% CA-based O-I and 15% CA-based O-II) in both loading scenarios, mainly attributable to the enhanced crack bridging effect resulting from the higher coarse aggregate content.

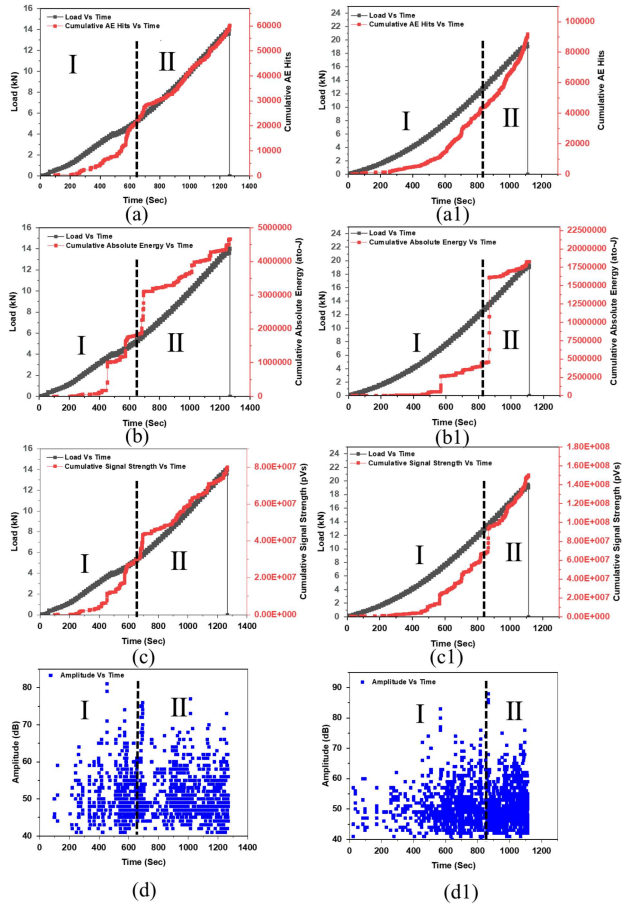

Figure 5: Variation in acoustic emission (AE) parameters for Mix 1 beams (0% CA Beams) a), b), c), d) O-I and a1), b1), c1), d1) O-II

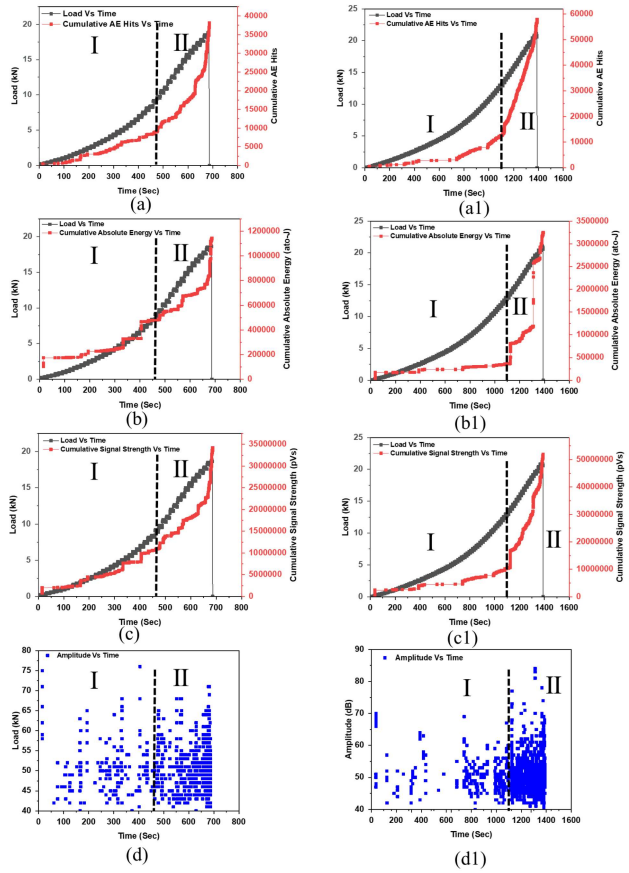

Figure 6: Variation in acoustic emission (AE) parameters for Mix 2 beams (5% CA Beams) a), b), c), d) O-I and a1), b1), c1), d1) O-II

This is well supported by the plots of load vs time as well. The difference in the pattern of 5% CA-based O-I beams may be due to voids present within the layer of a beam caused the early failure of the layer (See Fig. 6 a) and a1). The difference in the pattern for 15% CA-based O-II may be attributed to the early debonding of a layer, as a significant amount of energy released is observed in the micro-cracking zone around 380 seconds. The larger duration of a micro-cracking zone for the coarse aggregate-based printed specimens implies that the threshold from stable crack propagation to unstable fracture is greater. An additional significant observation is that no visible surface cracks are seen in this phase on any of the beams subjected to both loading orientations. Hence, all the AE parameters plots indicate the initiation and progression of micro-cracking inside the concrete only. Concerning the loading directions, the

duration of the micro-cracking phase is more significant for orientation II compared to orientation I, which may be attributed to the distribution of stress along the layer planes, allowing micro-cracks to form and propagate across a broader area before coalescing into macro-cracks. A similar pattern is observed in the case of notched beams as well.

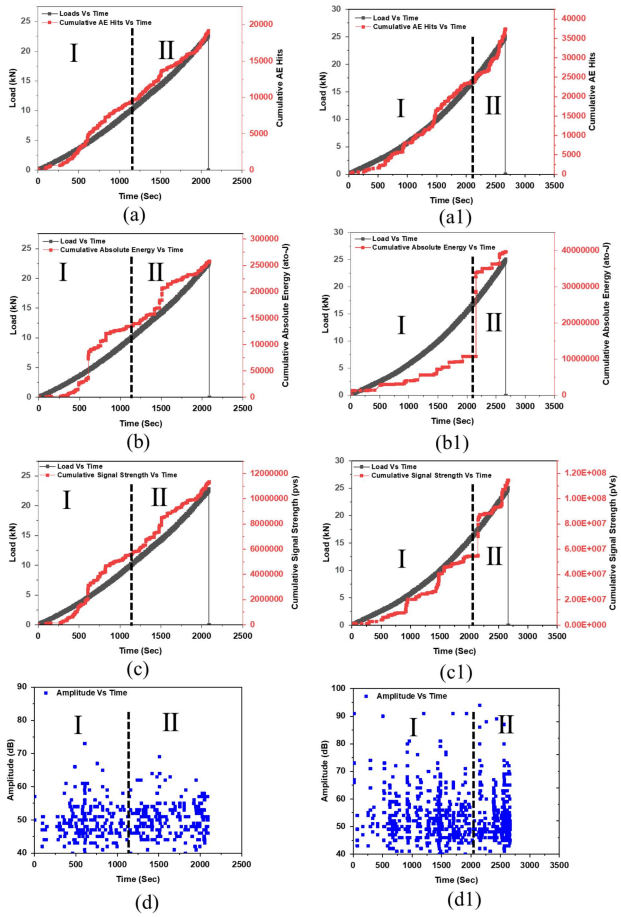

Figure 7: Variation in acoustic emission (AE) parameters for Mix 3 beams (10% CA Beams) a), b), c), d) O-I and a1), b1), c1), d1) O-II

3.3.2 Phase II

Further, with increasing loading on the beams beyond phase-I, a significant increase in cumulative acoustic emission hits (CAEH), cumulative signal strength (CSS), and cumulative absolute energy (CAE), accompanied by a larger average amplitude, is noted in both notched and unnotched beams. This signifies the emergence of significant acoustic emission activity due to the load increase, resulting in the macro-cracking phase. All the beams, being unreinforced, exhibited brittle behaviour. The duration of the macro-cracking phase for loading direction along orientation-I (O-I) is 618 sec for 0% CA-based beams, 226 sec for 5% CA-based beams, 941 sec for 10% CA-based beams, and 531 sec for 15% CA-based beams. For loading orientation-II (O-II), the durations are 283 seconds, 290 seconds, 938 seconds, and 661 seconds, respectively. With the exception of 0 % CA-based beams, all specimens utilizing coarse aggregates exhibit a greater duration for the macro-cracking phase in the loading direction O-II, whereas the macro-cracking duration remains nearly identical in the case of 10% CA-based beams. The same pattern is observed in the mix 4: 15% CA-based notch beams, which exhibit macro-cracking durations of 381 seconds and 485 seconds for O-I and O-II, respectively. Here also, notch effect dominance is observed and shows less duration than the identical 15% CA-based unnotch beams. Although the zone indicates the macro-cracking phase of the specimens, here also we have not observed any surface cracks and their widening. From the observation of AE signals, we inferred that all fracture widening occurred within the concrete matrix, including the expansion of interfacial transition zone (ITZ) cracks and interlayer debonding.

Moreover, at a brittle failure point, the highest CSS and CAE values are obtained and shown in Table 5. In the case of all the tested printed beams CSS and CAE values were observed higher for the loading along O-II as compared to O-I. As discussed above, the specimens with the loading orientation-II (lateral direction to the printing: O-II) show higher mechanical capacity in terms of strength. It is valid for both the mortar and the concrete specimens, with the concrete specimen showing higher strength, not only due to coarse aggregates within the layers but also because of better interlayer adhesion imparted by aggregate interlocking. The O-II configuration facilitates enhanced strain energy accumulation before failure due to the de-

layed emergence of the macro-crack. AE data also support this observation by demonstrating a longer duration of microcracking during the tests. Consequently, when the specimen undergoes a sudden brittle fracture, it releases significant strain energy, leading to an AE burst. This highlights the fundamental difference in failure behavior between mortar and coarse aggregate-based printed beams in different loading directions.

Table 5: Magnitudes of cumulative signal strength and cumulative absolute energy at failure point

Mix 1 beams	**O-I**	**O-II**
CSS (10^7 pV-Sec)	7.997	15.010
CAE (10^6 ato-J)	4.67	18.282
Mix 2 beams (5% CA)	**O-I**	**O-II**
CSS (10^7 pV-Sec)	3.422	5.190
CAE (10^6 ato-J)	1.144	3.249
Mix 3 beams (10% CA)	**O-I**	**O-II**
CSS (10^7 pV-Sec)	1.135	11.45
CAE (10^6 ato-J)	0.2579	39.68
Mix 4 beams (15% CA)	**O-I**	**O-II**
CSS (10^7 pV-Sec)	5.097	6.276
CAE (10^6 ato-J)	2.960	3.801
Mix 4 N beams (15% CA)	**O-I**	**O-II**
CSS (10^7 pV-Sec)	3.426	4.991
CAE (10^6 ato-J)	1.824	5.516

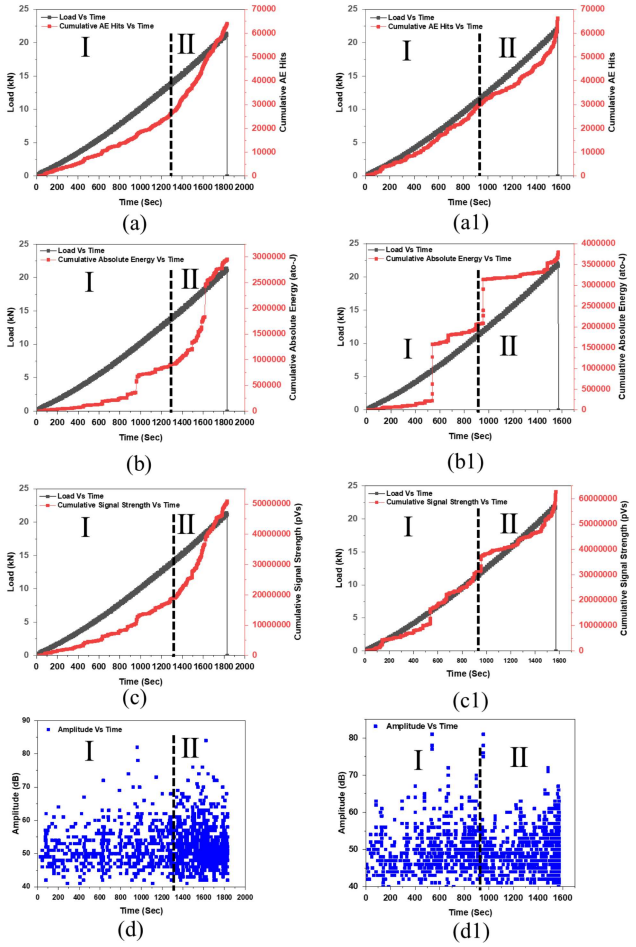

Figure 8: Variation in acoustic emission (AE) parameters for Mix 4 beams (15% CA Beams) a), b), c), d) O-I and a1), b1), c1), d1) O-II

A similar pattern is also observed in 15% coarse aggregate-based notch beams. The testing and failure patterns of the examined notched specimens are illustrated in Figure 9, 11. In the comparison between notched and unnotched beams, the unnotched beams exhibit superior CSS and CAE values, as well as the greatest load-carrying capability. The absence of a notch did not produce an initial stress field, resulting in many internal cracks that progressed through the whole depth and width of the printed beams. This led to an increased release of strain energy relative to notched specimens, indicating higher values of CSS and CAE [15].

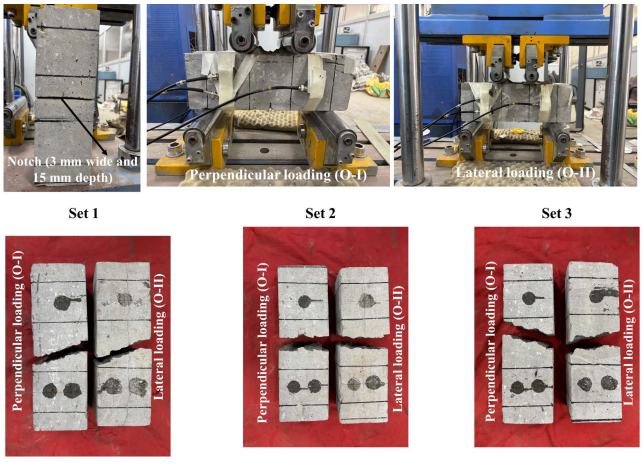

Figure 9: Fracture testing and tested specimens

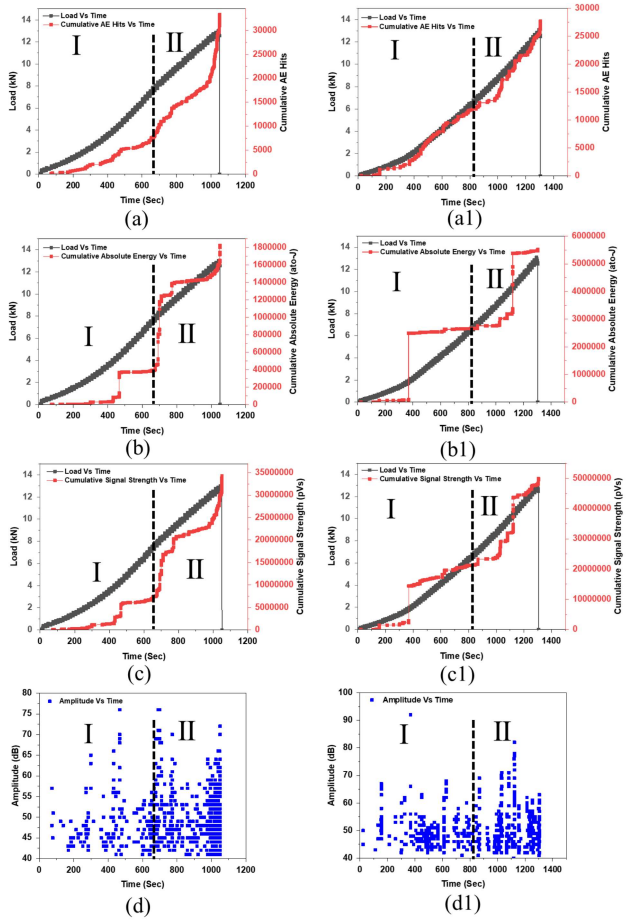

Figure 10: Variation in acoustic emission (AE) parameters for Mix 4 notched beams (15% CA Beams) a), b), c), d) O-I and a1), b1), c1), d1) O-II

Thus, from the present investigation, it can be concluded that the analysis of the AE parameters with respect to time along with the load vs. time plot can be effectively utilized to understand the initiation and propagation of cracks in the printed beams.

4 CONCLUSIONS

This study examines the flexural properties of coarse aggregate-based printed beams in comparison to mortar-based printed beams under various loading directions (O-I and O-II) utilizing the acoustic emission technique. For this investigation, four point-bending test is used. The first part of the study shows that for all notched and unnotched specimens, peak load and flexural strength are higher in the loading direction O-II (i.e. lateral to the printing direction). Furthermore, with variations in coarse aggregate content, an enhancement in flexural strength is observed in both loading directions, except at 15% coarse aggregate content. Despite variation in trend, it shows a higher flexural strength than the 0% CA-based printed specimens.

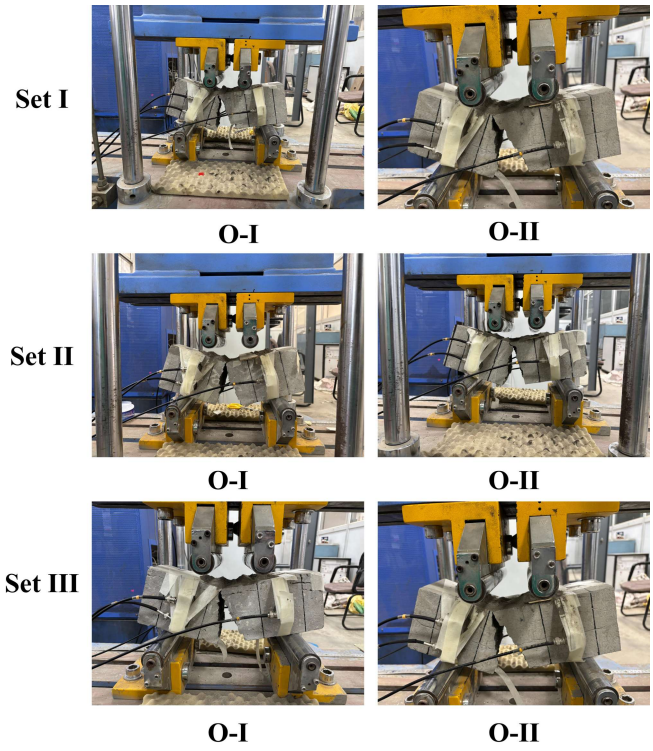

Figure 11: Fracture patterns for notched beams

The second segment of the study categorizes the loading zone into two sections, termed the micro-cracking zone and the macro-cracking zone. In both zones, we have not observed any surface cracking. In both loading directions, a rise in coarse aggregate content correlates with an extended length of the duration of the micro-cracking phase. A similar pattern is observed for the macro-cracking zone as well. This is attributable to the improvement in the bridging effect due to the coarse aggregates. At the same time, 15% CA-based printed notched beams show a lesser duration of micro-cracking phase as compared to 15% CA-based printed notched beams, which indicates a change in load-bearing capacity and failure pattern due to the inclusion of notch. The larger duration of

the micro-cracking zone implies that the threshold from stable crack propagation to unstable fracture is greater. In all the investigated specimens, higher values of CSS and CAE were observed at brittle failure points along O-II.

Despite these observations, some exceptions were observed in the trends. This study indicates the preliminary investigation of the flexural behaviour of coarse aggregate-based printed beams. Based on this initial study, it is concluded that AE parameters of cumulative AE hits and their amplitudes, cumulative signal strength and cumulative absolute energy are well indicative of different damage initiation modes and failure progression mechanisms in mortar and coarse aggregate-based printed beams. Further, a detailed study focussing on varying the number of layers in testing specimens and incorporating fibres along with coarse aggregates is in process.

REFERENCES

[1] Kaliyavaradhan, Senthil Kumar and Ambily, PS and Prem, Prabhat Ranjan and Ghodke, Swapnil Balasaheb, 2022. Test methods for 3D printable concrete. *Automation in construction* **142**:104529.

[2] Khoshnevis, Behrokh, 2004. Automated construction by contour crafting—related robotics and information technologies. *Automation in construction* **13**:5–19.

[3] Prem, Prabhat Ranjan and Ambily, PS and Kumar, Shankar and Ghodke, Swapnil Balasaheb, 2024. A theoretical model to predict the structural buildability of 3D printable concrete. *Mechanics of Time-Dependent Materials*:1–19.

[4] Wu, Yiwen and Liu, Chao and Liu, Huawei and Zhang, Zhenzi and He, Chunhui and Liu, Shuhua and Zhang, Rongfei and Wang, Youqiang and Bai, Guoliang, 2021. Study on the rheology and buildability of 3D printed concrete with recycled coarse aggregates. *Journal of Building Engineering***42**:103030.

[5] Zhang, Chao and Jia, Zijian and Wang, Xianggang and Jia, Lutao and Deng, Zhicong and Wang, Zhibin and Zhang, Yamei and Mechtcherine, Viktor, 2022. A two-phase design strategy based on the composite of mortar and coarse aggregate for 3D printable concrete with coarse aggregate. *Journal of Building Engineering* **54**:104672.

[6] Mohan, Manu K and Rahul, AV and De Schutter, Geert and Van Tittelboom, Kim, 2021. Extrusion-based concrete 3D printing from a material perspective: A state-of-the-art review. *Cement and Concrete Composites* **115**:103855.

[7] Skibicki, Szymon and Dvořák, Richard and Pazdera, Luboš and Topolář, Libor and Kocáb, Dalibor and Alexa, Martin and Cendrowski, Krzysztof and Hoffmann, Marcin, 2024. Anisotropic mechanical properties of 3D printed mortar determined by standard flexural and compression test and acoustic emission. *Construction and Building Materials* **452**:138957.

[8] Ingle, Vaibhav Vinod and Kaliyavaradhan, Senthil Kumar and Ambily, PS and Shekar, Deepadharshan, 2024. 3D printable concrete without chemical admixtures: Fresh and hardened properties. *Structural Concrete* **25**:365–378.

[9] Ding, Tao and Xiao, Jianzhuang and Zou, Shuai and Yu, Jiangtao, 2021. Flexural properties of 3D printed fibre-reinforced concrete with recycled sand. *Construction and Building Materials* **288**:1230774.

[10] Yue, JG and Beskos, DE and Feng, C and Wu, 2022. Hardened fracture characteristics of printed concrete using acoustic emission monitoring technique. *Construction and Building Materials* **361**:129684.

[11] IS 516 : Part 1 : Sec 1 : 2021: Hardened concrete methods of test part 1 testing of strength of hardened concrete sec-

tion 1 compressive,flexucal and split tensile strength (First Revision), *Bureau of Indian Standards*.

[12] Liu, Huawei and Liu, Chao and Wu, Yiwen and Bai, Guoliang and He, Chunhui and Yao, Yizhou and Zhang, Rongfei and Wang, Youqiang. 3D printing concrete with recycled coarse aggregates: The influence of pore structure on interlayer adhesion. *Cement and Concrete Composites* **134**:104742.

[13] Wolfs, RJM and Bos, FP and Salet, TAM, 2019. Hardened properties of 3D printed concrete: The influence of process parameters on interlayer adhesion. *Cement and Concrete Research* **119**:132–140.

[14] An, Dong and Zhang, YX and Yang, Richard. Incorporating coarse aggregates into 3D concrete printing from mixture design and process control to structural behaviours and practical applications: a review. *Virtual and Physical Prototyping* **19**:e2351154.

[15] Patil, Shilpa V and Mulla, Rubina R and Karkare, Bilavari S 2017. Fracture Characterization of Plain and Reinforced Concrete Beams Using Acoustic Emission Technique, *International Conference on Sensing, Diagnostics, Prognostics, and Control (SDPC)*; 143–148.